

Research Article

Modeling and Simulation of a Chemical Vapor Deposition

J. Geiser and M. Arab

Department of Mathematics, Humboldt University of Berlin, Unter den Linden 6, D-10099 Berlin, Germany

Correspondence should be addressed to J. Geiser, geiser@mathematik.hu-berlin.de

Received 29 November 2010; Accepted 17 January 2011

Academic Editor: Shuyu Sun

Copyright © 2011 J. Geiser and M. Arab. This is an open access article distributed under the Creative Commons Attribution License, which permits unrestricted use, distribution, and reproduction in any medium, provided the original work is properly cited.

We are motivated to model PE-CVD (plasma enhanced chemical vapor deposition) processes for metallic bipolar plates, and their optimization for depositing a heterogeneous layer on the metallic plate. Moreover a constraint to the deposition process is a very low pressure (nearly a vacuum) and a low temperature (about 400 K). The contribution of this paper is to derive a multiphysics system of multiple physics problems that includes some assumptions to simplify the complicate process and allows of deriving a computable mathematical model without neglecting the real-life processes. To model the gaseous transport in the apparatus we employ mobile gas phase streams, immobile and mobile phases in a chamber that is filled with porous medium (plasma layers). Numerical methods are discussed to solve such multi-scale and multi phase models and to obtain qualitative results for the delicate multiphysical processes in the chamber. We discuss a splitting analysis to couple such multiphysical problems. The verification of such a complicated model is done with real-life experiments for single species. Such numerical simulations help to economize on expensive physical experiments and obtain control mechanisms for the delicate deposition process.

1. Introduction

We motivate our research on producing high-temperature films by low-pressure deposition processes. Such deposition can only be achieved with plasma-enhanced processes; see [1]. In standard applications based on depositing binary systems such as TiN and TiC, new material classes arose. More delicate to deposit are nanolayered ternary metal-carbide or metal-nitride materials, including MAX-phase materials, while we have to control three species in the deposition process see [2].

To understand the growth of a thin film done by PE-CVD (plasma-enhanced chemical vapor deposition) processes, we have to model a complicated multiphysical process; see [3, 4].

Based on the process constraints, which are very low-pressure (nearly vacuum) and a low temperature (about 400 K), we can simplify the complicated model.

The delicate modeling part is to model the plasma, in which the deposition species, given as precursor gases, are transported; see [5]. We concentrate on plasma as an ionized medium, known as “cold” plasma or glow discharges; see [6, 7]. To model the gaseous transport of our deposition process in the cold plasma, a porous medium model with different permeable layers is an attractive simulation model; see [4]. In the chamber filled with an ionized plasma that is given as a porous medium, the gaseous transport involves several phases: mobile gas phase streams, and both immobile and adsorbed phases. For such processes, we present a multiphase and multispecies model; see [3, 8]. The species of the gaseous transport are MAX-phase materials; see [9–11], and we concentrate on Ti_3SiC_2 molecules, so we have Ti, Si, and C in the gas phases.

Further a porous medium model with permeable layers is an attractive simulation model also for the electric field in the chamber that is used to control the gaseous transport to the deposition area. Here the expertise of similar simulation models are used; see [12].

So the transport, chemical and sorption processes in a heterogeneous medium can be used to simulate species transport in a plasma-enhanced environment, controlled by pressure, temperature and by additional electric fields. Such modeling methods have been developed in recent years and are focused on producing high-temperature films; see [4].

Fundamental models of CVD processes employ detailed descriptions of fluid flow, mass transfer, heat transfer and chemical kinetics; see [13, 14].

While having a powerful deposition process in low-temperature and low-pressure regimes, we have also taken into account some drawbacks of such a process, which is driven with ionized plasma. Here, we deal with multicomponent problems with heavier and lighter species. Such conditions have consequences in slower (strongly adsorbed) or faster traveling (weakly adsorbed) species.

The contributions of this paper are to couple numerical methods that are developed to solve such multiscale and multiphase models and to obtain qualitative results on the delicate multiphysical processes in the chamber. Here splitting schemes are applied as an attractive tool to decouple delicate processes; see [15]. We apply and analyze splitting schemes, in a way that combines discretization methods for partial differential and ordinary differential equations; see [12, 15].

The immobile, adsorbed and reaction terms can be treated with fast Runge-Kutta solvers, whereas the mobile terms are convection-diffusion equations and are solved with splitting semi-implicit finite volume methods and characteristic methods, [16].

Such a sequential treatment of the partial differential equations and ordinary differential equations allow of saving computational time, while expensive implicit Runge-Kutta methods are reduced to the partial operators and fast explicit Runge-Kutta methods are for the ordinary operators of the multiphase model.

With various source terms we control the required concentration at the final deposition area.

Different kinetic parameters allow of simulating the different time scales of the heavier and lighter gaseous species.

The numerical results are verified with physical experiments and we discuss the applications to the production of so-called metallic bipolar plates.

This paper is outlined as follows. In Section 2, we present our mathematical model based on the multiphases. In Section 3, we present the underlying physical experiments for the model equations. In Section 4, we discuss discretization and solver methods with respect to their efficiency and accuracy. The numerical experiments are given in Section 5. In Section 6, we briefly summarize our results.

2. Mathematical Modeling

In the model we have included the following multiple physical processes, related to the deposition process:

- (i) flow field of the ionized plasma: Navier-Stokes equation; see [17],
- (ii) transport system of the species: mobile and immobile gaseous phases with Kinetically controlled adsorption (heavier and lighter species); see [4],
- (iii) electric field: Poisson equation; see [13, 18].

In the following we discuss the three models separately and combine all the models into a multiple physical model. We assume a two-dimensional domain of the apparatus with isotropic flow fields; see [17].

2.1. Flow Field

The conservation of momentum is given by (flow field: Navier-Stokes equation)

$$\begin{aligned} \frac{\partial}{\partial t} \mathbf{v} + \mathbf{v} \cdot \nabla \mathbf{v} &= -\nabla p, \quad \text{in } \Omega \times [0, t], \\ \mathbf{v}(\mathbf{x}, t) &= \mathbf{v}_0(\mathbf{x}), \quad \text{on } \Omega, \\ \mathbf{v}(\mathbf{x}, t) &= \mathbf{v}_1(\mathbf{x}, t), \quad \text{on } \partial\Omega \times [0, t], \end{aligned} \tag{2.1}$$

where \mathbf{v} is the velocity field, p the pressure, \mathbf{v}_0 the initial velocity field and the position vector $\mathbf{x} = (x_1, x_2)^t \in \Omega \subset \mathbb{R}^{2,+}$. Furthermore, we assume that the flow is divergence free and the pressure is predefined.

2.2. Transport Systems (Multiphase Equations)

We model the ionized plasma as an underlying medium in the chamber with mobile and immobile phases. Here transport in the plasma with gaseous species contain of mobile and immobile concentrations, [3]. For such a heterogenous plasma, we applied our expertise in modeling multiphase transport through a porous medium; see [2].

To amplify the modeling of the gaseous flow to the chamber which is filled with ionized plasma, we deal with the so-called far-field model based on a porous medium. Here the plasma can be modeled as a continuous flow [17], that has mobile and immobile phases; see [8].

We assume nearly a vacuum and a diffusion-dominated process, derived from the Knudsen diffusion, [19]. In such viscous flow regimes, we deal with small Knudsen numbers and a pressure of nearly zero. We discuss a modified model, including new system parameter spaces such as porosity and permeability, which describe the plasma flow through the reactor.

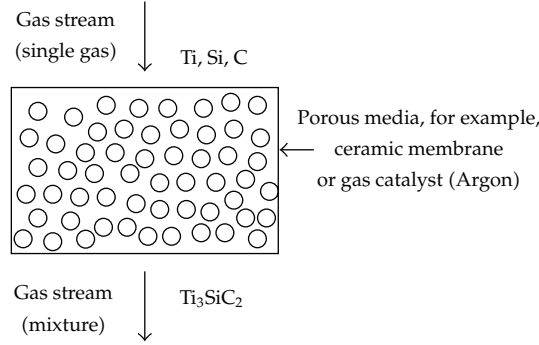


Figure 1: Chamber of the CVD apparatus.

In Figure 1, the chamber of the CVD apparatus is shown. It is modeled as a porous medium, where the porosity is given as the ratio between the void space and the total volume of the ceramic or bulk material:

$$\phi = \frac{V_v}{V_b}, \quad (2.2)$$

where V_v is the void space and V_b is the volume of the ceramic or bulk material.

For the one-phase model, the velocity v of the underlying fluid is calculated by Darcy's law and given by:

$$v = \frac{-\kappa}{\mu} \frac{\nabla p}{\phi}, \quad (2.3)$$

where κ is the permeability, ∇p is the pressure gradient, ϕ is the porosity and μ the dynamic viscosity.

To model a retarded gas concentration in the porous medium, we have to consider multiphases of the underlying fluid. The new model includes immobile and adsorbed phases, where the velocity of the fluid is zero and impermeable layers are given.

In the model, we consider both absorption and adsorption taking place simultaneously and with given exchange rates. Therefore we consider the effect of the gas concentrations' being incorporated into the porous medium.

We extend the model to two more phases:

- (i) immobile phase,
- (ii) adsorbed phase.

In Figure 2, the mobile and immobile phases of the gas concentration are shown in the macroscopic scale of the porous medium. Here the exchange rate between the mobile gas concentration and the immobile gas concentration control the flux to the medium.

In Figure 3, the mobile and adsorbed phases of the gas concentration are shown in the macroscopic scale of the porous medium. To be more detailed in the mobile and immobile phases, where the gas concentrations can be adsorbed or absorbed, we consider a further phase. Here the adsorption in the mobile and immobile phase is treated as a retardation and given by a permeability in such layers.

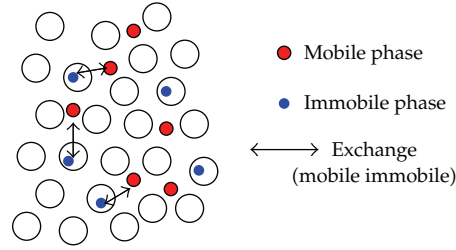


Figure 2: Mobile and immobile phase.

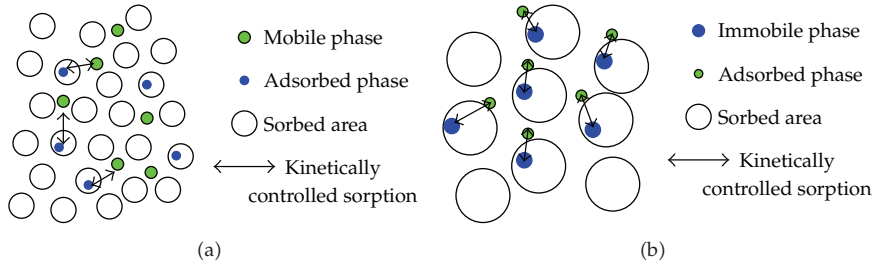


Figure 3: Mobile-adsorbed phase and immobile-adsorbed phase.

The model equations for the multiple phase equations are

$$\phi \partial_t c_i + \nabla \cdot \mathbf{F}_i = g(-c_i + c_{i,im}) + k_\alpha(-c_i + c_{i,ad}) - \lambda_{i,i} \phi c_i + \sum_{k=k(i)} \lambda_{i,k} \phi c_k + \tilde{Q}_i, \quad \text{in } \Omega \times [0, t], \quad (2.4)$$

$$\mathbf{F}_i = \mathbf{v}c_i - D^{e(i)} \nabla c_i + \eta \mathbf{E}c_i, \quad (2.5)$$

$$\phi \partial_t c_{i,im} = g(c_i - c_{i,im}) + k_\alpha(c_{i,im,ad} - c_{i,im}) - \lambda_{i,i} \phi c_{i,im} + \sum_{k=k(i)} \lambda_{i,k} \phi c_{k,im} + \tilde{Q}_{i,im}, \quad \text{in } \Omega \times [0, t], \quad (2.6)$$

$$\phi \partial_t c_{i,ad} = k_\alpha(c_i - c_{i,ad}) - \lambda_{i,i} \phi c_{i,ad} + \sum_{k=k(i)} \lambda_{i,k} \phi c_{k,ad} + \tilde{Q}_{i,ad}, \quad \text{in } \Omega \times [0, t], \quad (2.7)$$

$$\phi \partial_t c_{i,im,ad} = k_\alpha(c_{i,im} - c_{i,im,ad}) - \lambda_{i,i} \phi c_{i,im,ad} + \sum_{k=k(i)} \lambda_{i,k} \phi c_{k,im,ad} + \tilde{Q}_{i,im,ad}, \quad \text{in } \Omega \times [0, t], \quad (2.8)$$

$$c_i(\mathbf{x}, t) = c_{i,0}(\mathbf{x}), \quad c_{i,ad}(\mathbf{x}, t) = 0, \quad c_{i,im}(\mathbf{x}, t) = 0, \quad c_{i,im,ad}(\mathbf{x}, t) = 0, \quad \text{on } \Omega, \quad (2.9)$$

$$c_i(\mathbf{x}, t) = c_{i,1}(\mathbf{x}, t), \quad c_{i,ad}(\mathbf{x}, t) = 0, \quad c_{i,im}(\mathbf{x}, t) = 0, \quad c_{i,im,ad}(\mathbf{x}, t) = 0, \quad \text{on } \partial\Omega \times [0, t], \quad (2.10)$$

where the initial value is given as $c_{i,0}$ and we assume a Dirichlet boundary conditions with the function $c_{i,1}(\mathbf{x}, t)$ sufficiently smooth, all other initial and boundary conditions of the other phases are zero.

The parameters are given as:

ϕ : effective porosity [-],

c_i : concentration of the i th gaseous species in the plasma chamber,

$c_{i,im}$: concentration of the i th gaseous species in the immobile zones of the plasma chamber phase [mol/cm³],

\mathbf{v} : velocity through the chamber and porous substrate [20] [cm/nsec],

$D^{e(i)}$: element-specific diffusions-dispersions tensor [cm²/nsec],

$\lambda_{i,j}$: decay constant of the i th species [1/nsec],

\tilde{Q}_i : source term of the i th species [mol/(cm³nsec)],

g : exchange rate between the mobile and immobile concentration [1/nsec],

k_α : exchange rate between the mobile and adsorbed concentration or immobile and immobile adsorbed concentration (kinetic controlled sorption) [1/nsec],

\mathbf{E} : stationary electricfield in the apparatus [V/cm],

η : the mobility rate in the electricfield; see [13] [cm²/nsec],

with $i = 1, \dots, M$ and M denotes the number of components.

The parameters in (2.4) are further described; see also [12].

The four phases are treated in the full domain, such that we have a full coupling in time and space.

The effective porosity is denoted by ϕ and declares the portion of the porosities of the aquifer that is filled with plasma, and we assume a nearly fluid phase. The transport term is indicated by the Darcy velocity \mathbf{v} , that presents the flow direction and the absolute value of the plasma flux. The velocity field is divergence free. The decay constant of the i th species is denoted by λ_i . Thereby, $k(i)$ denotes the indices of the other species which react with species i .

2.3. Electric Field (Distribution)

In addition, in order to find the distribution of the electric field, it is necessary to solve the Poisson equation which relates the divergence of the local electric fields to the charge density [13], and is given by

$$\nabla \cdot \mathbf{E} = \frac{e}{\epsilon_0} \sum_{i=1}^n Z_i c_i, \quad (2.11)$$

where e is the charge of the electron, ϵ_0 the permittivity of the gas mixture, c_i the particle density of species i and Z_i the relative charge of species i ; see [21].

A general model for PECVD reactors is very complicated and we therefore simplify the model with some assumptions to obtain tractable problems.

(i) Predefined electric field \mathbf{E} respecting different predefined areas Ω_j , we apply:

$$\nabla \cdot \mathbf{E} \approx \frac{e}{\epsilon_0} \sum_{i=1}^n Z_i c_{\text{const},i}|_{\Omega_j}, \quad (2.12)$$

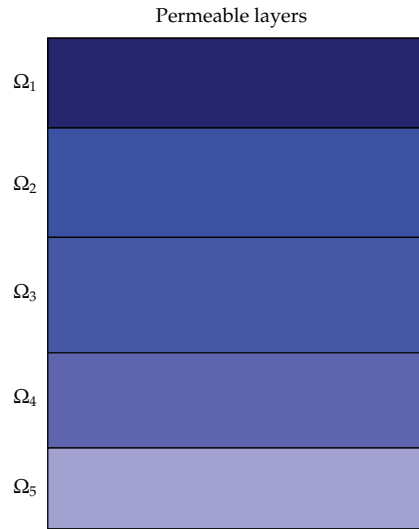


Figure 4: Electrical sectors in the domain of the apparatus.

where we assume that $c_i \approx c_{\text{const},i}$ for Ω_j is a constant particle density of species i in domain Ω_j with $j \in 1, \dots, m$ and m is the number of domains.

(ii) The plasma chemistry in the reactor is neglected.

2.4. Multiphysics Model

We derive the multiphysics model based on the multiphase and electric field model.

We start by developing the multiphysics model in the following steps:

- (i) transport system (multiphase model),
- (ii) electrical field is approximated by a permeable layer (field model),
- (iii) multiphysics model with multiphase transport and embedded electrical field.

We assume that the number of gas particles in the plasma atmosphere Ar (Argon) is low and the density of the particles can be treated as nearly constant.

Therefore, we can derive a constant field in each sector of the apparatus

$$\mathbf{E} \approx \mathbf{E}_{\Omega_j}, \quad (2.13)$$

where \mathbf{E}_{Ω_j} is constant and $\Omega_j \subset \Omega$ are sectors in the domain.

Such an electric field, see Figure 4, can be assumed in near-field experiments to be nearly homogeneous, where the field intensity is decreasing and can be assumed to be constant in small areas; see [4].

Next the idea is to embed the electric field into a porous medium model. A simplified model can be derived with given domain-dependent parameters and a retardation factor that includes the influence of the electric field.

First, the mobile phase equation (2.4) can be reformulated with retardation factor given by:

$$R_i \frac{\partial}{\partial t} c_i + \nabla \tilde{F}_i - R_i R_{g,i} = 0, \quad \text{in } \Omega \times [0, t], \quad (2.14)$$

$$\tilde{F}_i = \mathbf{v} c_i - D^{e(i)} \nabla c_i,$$

$$c_i(x, t) = c_{i,0}(x), \quad \text{on } \Omega, \quad (2.15)$$

$$c_i(x, t) = c_{i,1}(x, t), \quad \text{on } \partial\Omega \times [0, t],$$

where c_i is the particle density and \tilde{F}_i the flux of species i . $R_{g,i}$ is the reaction term of species i , meaning the right-hand side of (2.4), all other parameters as in (2.4)–(2.8). R_i is defined as a specific and constant Henry isotherm, called the retardation factor; see [22]. Such factors are known as sorption coefficients and model the rate between the mobile and immobile concentration, they are derived from experiments; see [23].

In a second step, we calculate the retardation factor, which is based on the influence of the electric field.

We subtract (2.4) from (2.14) and obtain

$$\nabla F_i = \frac{\nabla \tilde{F}_i}{R_i}. \quad (2.16)$$

We include the assumption of the electric field dependence of the domain parts and consider

$$\left(\frac{1}{R_i} - 1 \right) \nabla (\mathbf{v} - D^{e(i)} \nabla) c_i \approx \frac{e}{\epsilon_0} \sum_{k=1}^n Z_k c_{\text{const},k} |_{\Omega_j}, \quad \text{for } j = 1, \dots, m, \quad (2.17)$$

so we obtain the derivation of R_i for a specific domain $\Omega_j \subset \Omega$ and we have:

$$R_i = \left(\frac{e}{\epsilon_0} \sum_{k=1}^n Z_k c_{\text{const},k} |_{\Omega_j} \frac{1}{\nabla (\mathbf{v} - D^{e(i)} \nabla) c_i} + 1 \right)^{-1}, \quad \text{for } \Omega_j. \quad (2.18)$$

In the third step we add the equations (2.6)–(2.8) to the modified mobile phase equation (2.14) and we obtain the full coupled system.

Here the novel contribution is to derive a full coupled system of a multiphase and multiflow problem to include all the physical processes in the chamber. Such ideas have been developed and considered in fluid dynamical models for many years [24].

Remark 2.1. For the flow through the chamber, for which we assume a homogeneous medium and nonreactive plasma, we have considered a constant flow [1]. A further simplification is given by the very small porous substrate, for which we can assume the underlying velocity to a first approximation as constant [4].

Remark 2.2. For an in-stationary medium and reactive or ionized plasma, we have to take into account the relations of the electrons in thermal equilibrium. Such spatial variation can be considered by modeling the electron drift. Such modeling of the ionized plasma is done with Boltzmanns relation, [3].

3. Physical Experiments

The base of the experimental setup is the plasma reactor chamber of a NIST *GEC reference cell*. The spiral antenna of a hybrid ICP/CCP-RF plasma source was replaced by a double spiral antenna [25]. This reduces the asymmetry of the magnetic field due to the superposition of the induced fields of both antennas. Also, the power coupling to the plasma increases and enhances the efficiency of the source. A set of MKS mass flow controllers allows any defined mixture of gaseous precursors. Even the flows of liquid precursors with high vapour pressure is controlled by this system. All other liquid and all solid precursors will be directly transported to the chamber by a controlled carrier gas flow. Besides the precursor flow, the density can also be changed by varying the pressure inside the recipient. Controlling the pressure is achieved with a valve between the recipient and vacuum pumps. In addition, a heated and insulated substrate holder was mounted. Thus, a temperature up to 800°C and a bias voltage can be applied to the substrate. While the pressure and RF power determine the undirected particle energy (plasma temperature), the bias voltage adds, only to the charged particles, energy directed at the substrate. Apart from the pressure and RF power control, the degree of ionization and number as well as the size of the molecular fractions can be controlled.

Altogether, this setup provides as free process parameters:

- (i) pressure (typically 10^{-1} – 10^{-2} mbar),
- (ii) precursor composition (TMS, TMS + H₂, TMS + O₂),
- (iii) precursor flow rate (ranging from SCCM to SLM),
- (iv) RF Power (up to 1100 W),
- (v) substrate temperature (RT—800°C),
- (vi) bias voltage (DC, unipolar and bipolar pulsed, floating).

During all experiments, the process was observed by optical emission spectroscopy (OES) and mass spectroscopy (MS). The stoichiometry of the deposited films was analyzed *ex situ* in a scanning electron microscope (SEM) by energy dispersive X-ray analysis (EDX).

3.1. Realization of Physical Experiments

The following parameters were used for the physical experiments. Such a reduction allows of concentrating on the important flow and transport processes in the gas phase. Further, we apply the underlying mathematical model (far-field model, see Section 2.2) so that we can switch between physical and mathematical parameters (see Table 1).

- (1) Precursor: Tetramethylsilan (TMS).
- (2) Substrate: VA-Steel.
- (3) Film at substrate: SiC_x.

Table 1: The physical experiments with the real-life apparatus.

Test	P_R (mbar)	ϑ_S (C)	P_{plasma} (W)	ϕ (TMS) (SCCM)	$\phi(H_2)$ (SCCM)	Ratio (C:Si)	Mass (growth) (g)	Time (min)
080701-01-VA	$9.7E-2$	400	900	10.23	0	0.97811	0.00012	120
080718-01-VA	$1.1E-1$	400	900	10.00	0	1.00174	0.00050	130
080718-02-VA	$4.5E-2$	400	900	10.00	0	1.24811	0.00070	110
080618-01-VA	$4.3E-2$	400	500	10.23	0	1.32078	—	127
080716-01-VA	$1.1E-1$	400	500	10.00	0	1.42544	0.00250	120
080715-02-VA	$1.1E-1$	400	100	10.00	0	1.58872	0.00337	122
080804-01-VA	$4.5E-2$	400	100	10.00	0	2.91545	0.00356	129
080630-01-VA	$9.9E-2$	800	900	10.23	0	1.09116	0.00102	120
080807-01-VA	$4.5E-2$	800	900	10.00	0	1.18078	0.00118	120
080625-01-VA	$3.9E-2$	800	500	10.23	0	1.06373	—	120
080626-01-VA	$9.3E-2$	800	500	10.23	0	1.12818	0.00174	130
080806-01-VA	$4.8E-2$	800	100	10.00	0	1.73913	0.00219	121
080715-01-VA	$1.1E-1$	800	100	10.00	0	1.62467	0.00234	120
081016-01-VA	$1.0E-1$	600	300	10.00	0	1.72898	0.00321	123
081020-01-VA	$1.1E-1$	600	300	10.00	50	1.49075	0.00249	114
081028-01-VA	$1.1E-1$	600	300	10.00	15	1.53549	0.00273	120
081023-01-VA	$1.1E-1$	600	300	10.00	10	1.54278	0.00312	127
081027-01-VA	$1.1E-1$	600	300	10.00	5.5	1.55818	0.00277	126
081024-01-VA	$1.1E-1$	600	300	10.00	3.5	1.64367	0.00299	120
081022-01-VA	$1.0E-1$	600	300	10.00	2.5	1.69589	0.00318	127

We apply the parameters in Table 2 for interpolation of the substrate temperature.

For the substrate temperature and plasma power, we use the parameters in Table 3.

Remark 3.1. In the process, the temperature and power of the plasma is important and experiments show that these are significant parameters. Based on these parameters, we initialize the mathematical model and interpolate the flux and reaction parts.

4. Discretization and Solver Methods

We distinguish between the mobile and immobile phases. Here the mobile phases are parabolic partial differential equations and the immobile phases are ordinary differential equations. So for the space-discretization of the PDE's we apply finite volume methods as mass-conserved discretization schemes and for the time-discretization of the PDE's and ODE's we apply Runge-Kutta methods.

So first we discretize in space, while we then apply a splitting method, taking into account the different matrices.

Table 2

Temperature (C)	Ratio (SiC:C)
400	2.4:1
600	1.5:1
700	1.211:1
800	1.1:1

Table 3

Temperature (C)	Power (W)	Ratio (SiC:C)
400	900	1:0.97
400	500	1.3:1
800	900	1.18:1

4.1. Spatial Discretization

We deal with the transport part of the mobile phase, see (2.14):

$$R_i \frac{\partial}{\partial t} c_i + \nabla \tilde{F}_i = 0, \quad \text{in } \Omega \times [0, t], \quad (4.1)$$

$$\tilde{F}_i = \mathbf{v}c_i - D^{e(i)} \nabla c_i,$$

$$c_i(x, t) = c_{i,0}(x), \quad \text{on } \Omega, \quad (4.2)$$

$$c_i(x, t) = c_{i,1}(x, t), \quad \text{on } \partial\Omega \times [0, t],$$

For the convection part, we use a piecewise constant finite volume method with upwind discretization; see [26]. For the diffusion-dispersion part, we also apply a finite volume method and we assume the boundary values are denoted by $\mathbf{n} \cdot D^{e(i)} \nabla c_i(x, t) = 0$, where $x \in \Gamma$ is the boundary $\Gamma = \partial\Omega$; compare with [27]. The initial conditions are given by $c_i(x, 0) = c_{i,0}(x)$.

We integrate (4.1) over space and obtain

$$\int_{\Omega_j} R_i \frac{\partial}{\partial t} c_i \, dx = \int_{\Omega_j} \nabla \cdot \left(-\mathbf{v}c_i + D^{e(i)} \nabla c_i \right) dx. \quad (4.3)$$

The time integration is done later in the decomposition method with implicit-explicit Runge-Kutta methods. Further the diffusion-dispersion term is lumped; compare with [12]. Equation (4.3) is discretized over space using Green's formula

$$V_j R_i \frac{\partial}{\partial t} c_i \, dx = \int_{\Gamma_j} \mathbf{n} \cdot \left(-\mathbf{v}c_i + D^{e(i)} \nabla c_i \right) d\gamma, \quad (4.4)$$

where Γ_j is the boundary of the finite volume cell Ω_j and V_{uj} is the volume of the cell j . We use the approximation in space; see [12].

The spatial integration for the diffusion part (4.4) is done by the mid-point rule over its finite boundaries and the convection part is done with a flux limiter and we obtain:

$$V_j R_i \frac{\partial}{\partial t} c_{i,j} = \sum_{e \in \Lambda_j} \mathbf{n}^e \nabla \mathbf{v} c_i^e d\gamma + \sum_{e \in \Lambda_j} \sum_{k \in \Lambda_j^e} |\Gamma_{jk}^e| \mathbf{n}_{jk}^e \cdot D_{jk}^e \nabla c_{i,jk}^e, \quad (4.5)$$

where $|\Gamma_{jk}^e|$ is the length of the boundary element Γ_{jk}^e . The gradients are calculated with the piecewise finite-element function ϕ_l .

We decide to discretize the ux with an up-winding scheme and obtain the following discretization for the convection part:

$$F_{j,e} = \begin{cases} \mathbf{v}_{j,e} c_{i,j}, & \text{if } v_{j,e} \geq 0, \\ \mathbf{v}_{j,e} c_{i,k}, & \text{if } v_{j,e} < 0, \end{cases} \quad (4.6)$$

where $v_{j,e} = \int_e \mathbf{v} \cdot \mathbf{n}_{j,e} ds$.

We obtain for the diffusion part:

$$\nabla c_{jk}^e = \sum_{l \in \Lambda^e} c_l \nabla \phi_l(\mathbf{x}_{jk}^e). \quad (4.7)$$

We get, using difference notation for the neighbour points j and l ; compare with [28], the full semi-discretization:

$$V_j R_i \frac{\partial}{\partial t} c_{i,j} = \sum_{e \in \Lambda_j} F_{j,e} + \sum_{e \in \Lambda_j} \sum_{l \in \Lambda^e \setminus \{j\}} \left(\sum_{k \in \Lambda_j^e} |\Gamma_{jk}^e| \mathbf{n}_{jk}^e \cdot D_{jk}^e \nabla \phi_l(\mathbf{x}_{jk}^e) \right) (c_j - c_l), \quad (4.8)$$

where $j = 1, \dots, m$.

Remark 4.1. For higher-order discretization of the convection equation, we apply a reconstruction which is based on Godunov's method. We apply a limiter function that fulfills the local min-max property. The method is explained in [26]. The linear polynomials are reconstructed by the element-wise gradient and are given by

$$\begin{aligned} u(x_j) &= c_j, \\ \nabla u|_{V_j} &= \frac{1}{V_j} \sum_{e=1}^E \int_{T^e \cap \Omega_j} \nabla c \, dx, \quad \text{with } j = 1, \dots, I. \end{aligned} \quad (4.9)$$

The piecewise linear functions are denoted by

$$u_{jk} = c_j + \varphi_j \nabla u|_{V_j}(x_{jk} - x_j), \quad \text{with } j = 1, \dots, I, \quad (4.10)$$

where $\varphi_j \in (0,1)$ is the limiter function and it fulfills the discrete minimum-maximum property, as described in [26].

4.2. Splitting Method to Couple Mobile, Immobile, and Adsorbed Parts

The motivation of the splitting method is the following observations.

- (i) The mobile phase is semidiscretized with fast finite volume methods and can be stored in a stiffness matrix. We achieve large time steps, if we consider implicit Runge-Kutta methods of lower order (e.g., implicit Euler) as a time discretization method.
- (ii) The immobile, adsorbed, and immobile-adsorbed phases are pure ordinary differential equations and each is cheap to solve with explicit Runge-Kutta schemes.
- (iii) The ODEs can be seen as perturbations and are solved explicitly in the iterative scheme.

For the full equation we use the following matrix notation:

$$\begin{aligned}
 \partial_t \mathbf{c} &= A_1 \mathbf{c} + A_2 \mathbf{c} + B_1(\mathbf{c} - \mathbf{c}_{im}) + B_2(\mathbf{c} - \mathbf{c}_{ad}) + \mathbf{Q}, \\
 \partial_t \mathbf{c}_{im} &= A_2 \mathbf{c}_{im} + B_1(\mathbf{c}_{im} - \mathbf{c}) + B_2(\mathbf{c}_{im} - \mathbf{c}_{im,ad}) + \mathbf{Q}_{im}, \\
 \partial_t \mathbf{c}_{ad} &= A_2 \mathbf{c}_{ad} + B_2(\mathbf{c}_{ad} - \mathbf{c}) + \mathbf{Q}_{ad}, \\
 \partial_t \mathbf{c}_{im,ad} &= A_2 \mathbf{c}_{im,ad} + B_2(\mathbf{c}_{im,ad} - \mathbf{c}_{im}) + \mathbf{Q}_{im,ad},
 \end{aligned} \tag{4.11}$$

where $\mathbf{c} = (c_1, \dots, c_m)^T$ is the spatial discretized concentration in the mobile phase, see (2.4), and $\mathbf{c}_{im} = (c_{1,im}, \dots, c_{m,im})^T$ is the concentration in the immobile phase, and similarly for the other phase concentrations. A_1 is the stiffness matrix of (2.4), A_2 is the reaction matrix of the right-hand side of (2.4), B_1 and B_2 are diagonal matrices with entries the immobile and kinetic parameters, see (2.7) and (2.8).

Furthermore $\mathbf{Q}, \dots, \mathbf{Q}_{im,ad}$ are the spatially discretized source vectors.

Now we have the following ordinary differential equation:

$$\partial_t \mathbf{C} = \begin{pmatrix} A_1 + A_2 + B_1 + B_2 & -B_1 & -B_2 & 0 \\ -B_1 & A_2 + B_1 + B_2 & 0 & -B_2 \\ -B_2 & 0 & A_2 + B_2 & 0 \\ 0 & -B_2 & 0 & A_2 + B_2 \end{pmatrix} \mathbf{C} + \tilde{\mathbf{Q}}, \tag{4.12}$$

where $\mathbf{C} = (\mathbf{c}, \mathbf{c}_{im}, \mathbf{c}_{ad}, \mathbf{c}_{im,ad})^T$ and the right-hand side is $\tilde{\mathbf{Q}} = (\mathbf{Q}, \mathbf{Q}_{im}, \mathbf{Q}_{ad}, \mathbf{Q}_{im,ad})^T$.

For such an equation we apply the decomposition of the matrices

$$\begin{aligned}
 \partial_t \mathbf{C} &= \tilde{A} \mathbf{C} + \tilde{\mathbf{Q}}, \\
 \partial_t \mathbf{C} &= \tilde{A}_1 \mathbf{C} + \tilde{A}_2 \mathbf{C} + \tilde{\mathbf{Q}},
 \end{aligned} \tag{4.13}$$

where

$$\tilde{A}_1 = \begin{pmatrix} A_1 + A_2 & 0 & 0 & 0 \\ 0 & A_2 & 0 & 0 \\ 0 & 0 & A_2 & 0 \\ 0 & 0 & 0 & A_2 \end{pmatrix}, \quad \tilde{A}_2 = \begin{pmatrix} B_1 + B_2 & -B_1 & -B_2 & 0 \\ -B_1 & B_1 + B_2 & 0 & -B_2 \\ -B_2 & 0 & B_2 & 0 \\ 0 & -B_2 & 0 & B_2 \end{pmatrix}. \quad (4.14)$$

This system of equations is numerically solved by an iterative scheme.

Algorithm 4.2. We divide our time interval $[0, T]$ into subintervals $[t^n, t^{n+1}]$, where $n = 0, 1, \dots, N$, $t^0 = 0$ and $t^N = T$.

We start with $n = 0$.

(1) The initial conditions are given by $\mathbf{C}_0(t^{n+1}) = \mathbf{C}(t^n)$. We start with $k = 0$.

(2) Compute the fixed-point iteration scheme given by

$$\partial_t \mathbf{C}^k = \tilde{A}_1 \mathbf{C}^k + \tilde{A}_2 \mathbf{C}^{k-1} + \tilde{\mathbf{Q}}, \quad (4.15)$$

where k is the iteration index; see [29]. For the time integration, we apply Runge-Kutta methods as ODE solvers; see [30, 31].

(3) The stop criterion for the time interval t^n, t^{n+1} is given by

$$\|\mathbf{C}^k(t^{n+1}) - \mathbf{C}^{k-1}(t^{n+1})\| \leq \text{err}, \quad (4.16)$$

where $\|\cdot\|$ is the maximum norm over all components of the solution vector. err is a given error tolerance, for example, $\text{err} = 10^{-4}$.

If (4.16) is fulfilled, we have the result

$$\mathbf{C}(t^{n+1}) = \mathbf{C}^k(t^{n+1}). \quad (4.17)$$

If $n = N$ (which means we reach the maximum iterative steps), then we stop and are done.

If (4.16) is not fulfilled, we do $k = k + 1$ and go to (2).

The error analysis of the schemes is given in the following theorem.

Theorem 4.3. Let $A, B \in \mathcal{L}(\mathbf{X})$ be given linear bounded operators in a Banach space $\mathcal{L}(\mathbf{X})$. We consider the abstract Cauchy problem

$$\begin{aligned} \partial_t \mathbf{C}(t) &= \tilde{A} \mathbf{C}(t) + \tilde{B} \mathbf{C}(t), \quad t_n \leq t \leq t_{n+1}, \\ \mathbf{C}(t_n) &= \mathbf{C}_n, \quad \text{for } n = 1, \dots, N, \end{aligned} \quad (4.18)$$

where $t_1 = 0$ and the final time is $t_N = T \in \mathbb{R}^+$. Then problem (4.18) has a unique solution. For finite steps with time size $\tau_n = t^{n+1} - t^n$, the iteration (4.15) for $k = 1, 2, \dots, q$ is consistent with an order of consistency $\mathcal{O}(\tau_n^q)$.

Proof. The outline of the proof is given in [15]. □

5. Experiments for the Multiple Phase Model

In the following subsections, we present our experiments based on the mobile, immobile and adsorbed gaseous phases.

We contribute ideas to obtain an optimal layer deposition, which is based on the PE-CVD process, while different additional phases are considered, for example, plasma and precursor media.

The main contributions are an optimal collection of point sources, line sources or moving sources to cover the deposition area, with respect to the remainder concentration in the immobile and adsorbed phases.

We simulate the deposition process with our boundary value solver algorithms and could deal with many different conditions that might be impossible for physical experiments. Such simulation results may benefit the physical experiment and give new ideas to optimize such deposition problems of a complicated physical process.

5.1. Verification of the Code with Analytical Solutions

In the verification of our software code UG; see [32], we apply the multiphase model (2.4) and (2.6) with the following parameters.

We use ascending parameters for the retardation factors. The retardation factors are given by $R_1 = 16$, $R_2 = 8$, $R_3 = 4$, R_4 . The reaction factors are given by $\lambda_1 = 0.4$, $\lambda_2 = 0.3$, $\lambda_3 = 0.2$, $\lambda_0 = 0$.

The initial conditions for the mobile phase are given by

$$c_i(x, 0) = \begin{cases} a_i x + b_i, & x \in (x_1, x_2), \\ 0, & \text{otherwise,} \end{cases} \quad (5.1)$$

where the parameters are given by $x_1 = 0.0$, $x_2 = 1.0$, $a_1 = 1.0$, $b_1 = 1.0$, $a_2 = -1.0$, $b_2 = 1.0$, $a_3 = 1.0$, $b_3 = 0.0$, $a_4 = 2.0$, $b_4 = 1.0$.

The mobile-immobile exchange rate is $g = 0.5$.

The initial conditions for the immobile concentrations are $c_{im}(0) = (1, 1, 1, 1)^t$.

For the time integration method we apply a fourth-order Runge-Kutta method and we apply $k = 1, \dots, 4$ iterative steps for the solver scheme.

The errors are given by

$$\text{err}_{i,j} = \sum_{k=1}^N |u_{i, \text{coupled}, j-1}(x_k, t) - u_{i, \text{coupled}, j}(x_k, t)|, \quad (5.2)$$

where $x_k = (k-1)\Delta x$, $k = 0, \dots, N$, $\Delta x = 0.01$, $N = 1000$, and $j = 2, 3, 4, 5$.

The solutions of the species are given in Figures 5 and 6.

Remark 5.1. The iterative scheme reduced the amount of numerical work to couple the mobile and immobile equations. We obtain more accurate results by using 3-4 iterative steps. Such schemes help the flexibility in coupling model equations by reducing the amount of recoding needed. More accuracy can be simply achieved with more iterative steps.

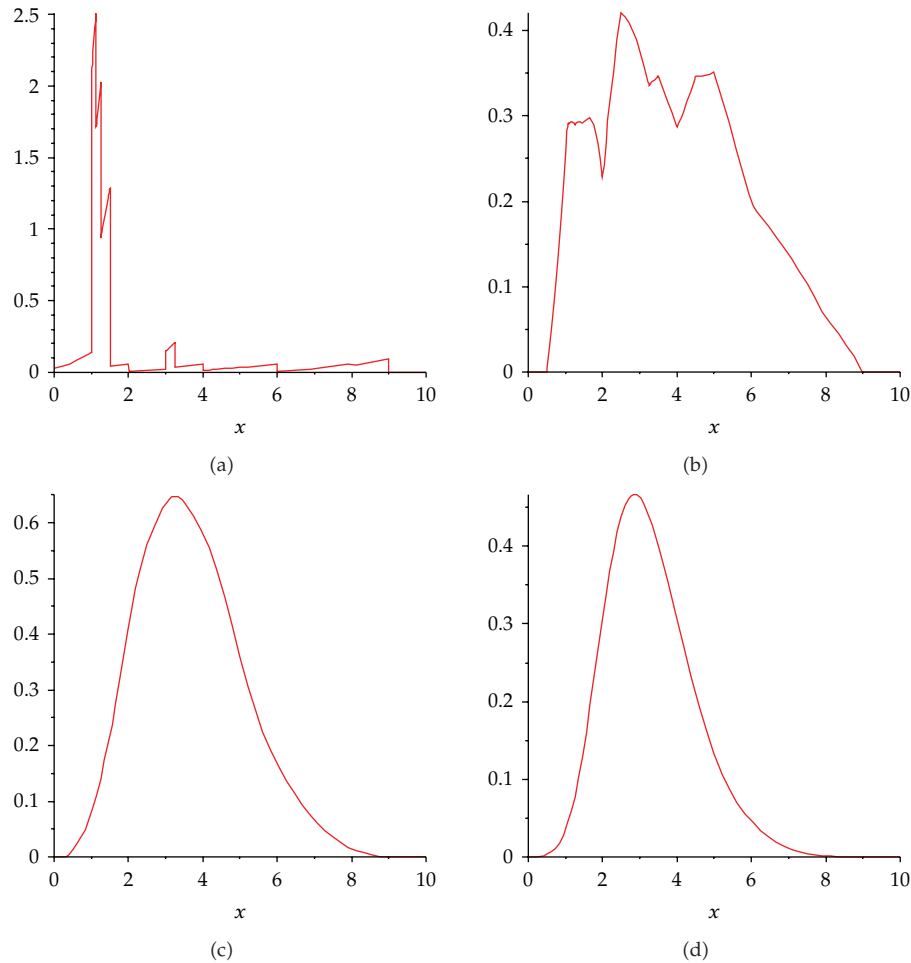


Figure 5: Experiment with the coupled model for the mobile solutions c_{im} , with $j = 2$ and $j = 4$ iteration steps at time point $t = 8$.

Table 4: Physical and mathematical parameters.

Physical parameter	Mathematical parameter
Temperature, pressure, power	Velocity, diffusion, reaction
T, p, W	V, D, λ

5.2. Verification of the Model with Physical Experiments

For the next experiments, we have the following parameters of the model, discretization, and solver methods.

We apply interpolation and regression methods to couple the physical parameters that were discussed in Section 3, to the mathematical parameters, see Figure 7 and Table 4.

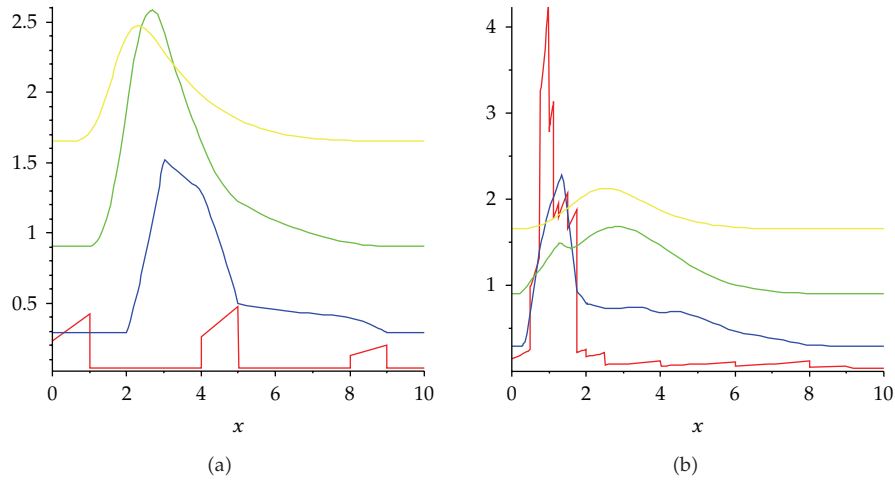


Figure 6: Experiment with the coupled model for the immobile solutions c_{im} , with $j = 2$ and $j = 4$ iteration steps at time point $t = 8$.

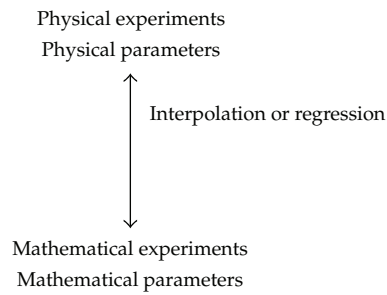


Figure 7: Coupling of physical and mathematical parameter space.

Parameters of (2.4)–(2.8)

In Table 8, we list the parameters for our simulation tool UG; see [32]. The software toolbox has a flexible user interface to allow a large number of numerical experiments and approximations using the known physical parameters.

Discretization Method

Finite-volume method of 2nd order is shown in Table 9.

Time Discretization Method

Crank-Nicolson method (2nd order).

Solver Method

In Tables 10 and 11, we deal with test examples which are approximations of physical experiments.

Table 5: Computed and experimental fitted parameters from UG simulations.

T	λ (fitted)	λ (interpolated)	Ratio (SiC:C) (computed with UG)
400	$1/2 \cdot 10^{-8}$	—	2.4:1
500	—	$0.35 \cdot 10^{-8}$	1.85:1
600	$1/4 \cdot 10^{-8}$	—	1.5:1
700	—	$0.171 \cdot 10^{-8}$	1.211:1
800	$1/8 \cdot 10^{-8}$	—	1.1:1

Table 6: Parameters of source concentration.

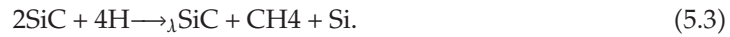
Point source at position	$(x, y) = (50, 20)$
Starting point of source concentration	$t_{\text{start}} = 0.0$
End point of source concentration	$t_{\text{end}} = 110^8$
Amount of permanent source concentration	$c_{\text{source}} = 1.0$
Number of time steps	25

Table 7: Rate of concentration.

Rate
$\text{SiC}_{\text{source, max}} : \text{SiC}_{\text{target, max}} = 9 \cdot 10^6 : 6.5 \cdot 10^6 = 1.38$

Numerical Experiment

In the test example, we deal with the following reaction:



Here, we have physical experiments and approximate temperature parameters $T = 400, 600, 800$.

We compute the SiC:C ratio at a given temperature $T = 400, 600, 800$ with the UG program and fit to the parameter λ .

We use a Lagrangian formula to compute λ for the new temperatures $T = 500, 700$ and apply the ratio of the simulated new parameters (Table 5). These numerical results are used to initialise the physical experiments in Table 12.

One Source

See Table 6.

In Figure 8, we present the concentration of one point source at $(50, 20)$ with number of time steps equal to 25.

In Figure 9, we show the deposition rates of one point source at $(50, 20)$, with number of time steps equal to 25.

Remark 5.2. In the numerical experiments, we could approximate the physical experiments and obtain the same deposition rates for the Si:C deposition. Therefore, the model allows of making predictions about future deposition rates with various parameters. Such numerical experiments can replace expensive physical experiments and allow of restricting them to more special cases.

Table 8: Model parameters.

Density	$\rho = 1.0$
Mobile porosity	$\phi = 0.333$
Immobile porosity	0.333
Diffusion	$D = 0.0$
Longitudinal dispersion	$\alpha_L = 0.0$
Transversal dispersion	$\alpha_T = 0.00$
Retardation factor	$R = 100e - 4$ (Henry rate)
Velocity field	$\mathbf{v} = (0.0, -4.0 \cdot 10^{-8})^t$
Decay rate of species of 1st EX	$\lambda_{AB} = 1 \cdot 10^{-68}$
Decay rate of species of 2nd EX	$\lambda_{AB} = 2 \cdot 10^{-8}, \lambda_{BNN} = 1 \cdot 10^{-68}$
Decay rate of species of 3rd EX	$\lambda_{AB} = 0.25 \cdot 10^{-8}, \lambda_{CB} = 0.5 \cdot 10^{-8}$
Geometry (2D domain)	$\Omega = [0, 100] \times [0, 100]$
Boundary	Neumann boundary at top, left, and right boundaries Outflow boundary at bottom boundary

Table 9: Spatial discretization parameters.

Spatial step size	$\Delta x_{\min} = 1.56, \Delta x_{\max} = 2.21$
Refined levels	6
Limiter	Slope limiter
Test functions	Linear test function reconstructed with neighbour gradients

Table 10: Spatial discretization parameters.

Initial time step	$\Delta t_{\text{init}} = 5 \cdot 10^7$
Controlled time step	$\Delta t_{\text{max}} = 1.298 \cdot 10^7, \Delta t_{\text{min}} = 1.158 \cdot 10^7$
Number of time steps time step control	100, 80, 30, 25 time steps are controlled with the Courant number $\text{CFL}_{\text{max}} = 1$

Table 11: Solver methods and their parameters.

Solver	BiCGstab (Bi conjugate gradient method)
Preconditioner	Geometric multigrid method
Smoother	Gauss-Seidel method as smoothers for the multigrid method
Basic level	0
Initial grid	Uniform grid with 2 elements
Maximum level	6
Finest grid	Uniform grid with 8192 elements

Table 12: L_2 -norm of the solution with refinements and CPU time.

Max · level	L_2 · norm	Max · norm	Elements	CPU · time	Time steps
6	1.6232 + 09	7.5026 + 07	8192	1.1 min	19
7	1.6222 + 09	7.7068 + 07	32768	3.55 min	19
8	1.6155 + 09	7.6753 + 07	131072	15.7 min	19
9	1.6137 + 09	7.6267 + 07	524288	59.55 min	19

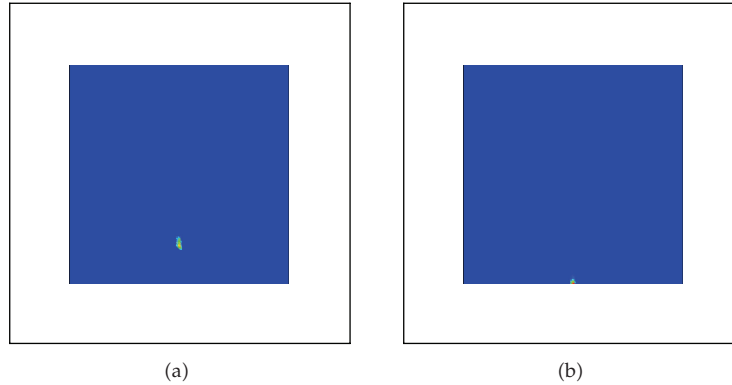


Figure 8: One point source at (50,20) with 25 time steps, full concentration is given in red and zero concentration with blue.

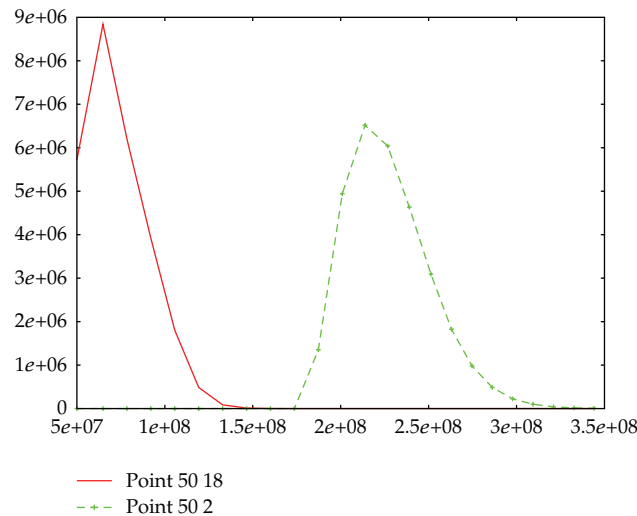


Figure 9: Deposition rates for one point source at (50,20), with 25 time steps (x -axis: time scale in (nsec), y -axis: deposition rate in (mol/nsec)).

5.3. Experiments with Full Model ($\alpha = 4 \cdot 10^{-14}$ and Immobile Rate $g = 8 \cdot 10^{-14}$)

In this experiment, we have taken into account the full model and verify with the previous simpler model equations that are verified by physical experiments.

Such novel experiments allow of giving prognoses of which direction of model modification can be important for future diagnostics of physical experiments.

We have the following outline of the experiment.

The exchange in the following experiments of the carbon (C) species between the mobile and immobile concentrations is very low, it is about $g = 8 \cdot 10^{-14}$, we assume less activities in the plasma environment. Further the exchange between the mobile and adsorbed mobile concentrations is also very low, it is about $\alpha = 4 \cdot 10^{-14}$, also the exchange rates between the immobile and adsorbed immobile concentration is the same as in the mobile and adsorbed mobile phases.

In previous experiments; see [33], we obtained optimal deposition results by combining multiple point sources which can be moved in the spatial directions (moving sources). Further we could approximate the physical results, while using mobile and immobile phase models.

In this experiment we increase the model to four phases in order to predict the delicate adsorbed regions. Physicists called such regions lost deposition areas, where the deposition material vanishes into the apparatus; see [25].

We taken into account 11 point sources at the positions $Y = 20, 21, 22, 23, 24, 25, 26, 27, 28, 29, 30$, and these sources are moving in the X direction in equal spatial steps with 15.

The concentration of each source in each step is equal to 1. The starting movement of X is given with $50 \rightarrow 35 \rightarrow 20 \rightarrow 35 \rightarrow 50 \rightarrow 65 \rightarrow 80 \rightarrow 65 \rightarrow 50$.

In Figure 10, we present the experiment with 11 moving sources at the positions in four phases. We obtain high depositions in the mobile phase, while we have only marginal depositions in the immobile and adsorbed phases.

Here the important observations to give a measurement of the deposition are the various deposition rates in the different phases.

In Figure 11, we present the deposition rate of mobile concentration of 11 moving sources moving in the X -direction in steps of 15: X moves from $50 \rightarrow 35 \rightarrow 20 \rightarrow 35 \rightarrow 50 \rightarrow 65 \rightarrow 80 \rightarrow 65 \rightarrow 50$, with the number of time steps equal to 25.

In see Table 12, we discuss the CPU time for the spatial refinements. We consider the L_2 -norm of the solution and obtain convergent results of the solutions.

Remark 5.3. With moving sources we gain improved deposition rates, this was also observed in [33]. Nevertheless the remaining concentration in the immobile and adsorbed phases are important for seeing the lost areas. In Figure 11, the maximum deposition rate of carbon in the mobile phase is $1.2 \cdot 10^8$ [mol], while the maximum lost deposition rate in the other phases are at least 18000 [mol]. So in the immobile and adsorbed phases we lost only 0.00018 percent concentration of the deposition material. This may seem to be neglectable, but we have considered only 1 [sec] deposition time, while a full cycle of deposition could be 1000 [sec]. Therefore we lost about 10% of the concentration in the apparatus, which is immense. Due to this fact, such models are important for foreseeing the percentage of lost concentration. One of the simulation results is the usage of higher amount of depositon material, that is, the higher amount of the underlying precursor gases are used to overcome the lost of concentrations in the apparatus. The second result is to consider more detailed models to predict the influence of the multiphases of the underlying gaseous species.

6. Conclusions and Discussions

We have presented a continuous model for the multiple phases, we assumed gaseous behaviour with exchange rates to adsorbed and immobile phases at very low-pressure and low temperature while dealing with catalyst processes, for example, plasma environment and precursor gases. We have to take into account the remaining gas concentrations in each processes. Such detailed modelling allows of seeing the delicate retardation and sorption processes of the underlying plasma medium. From the methodology side of the numerical simulations, the contributions were to decouple the multiphase problem into single-phase problems, where each single problem can be solved with more accuracy. The iterative schemes allows of coupling the simpler equations and for each additional iterative step, we could reduce the splitting error. Such iterative methods allow of accelerating the solver process of multiphase problems.

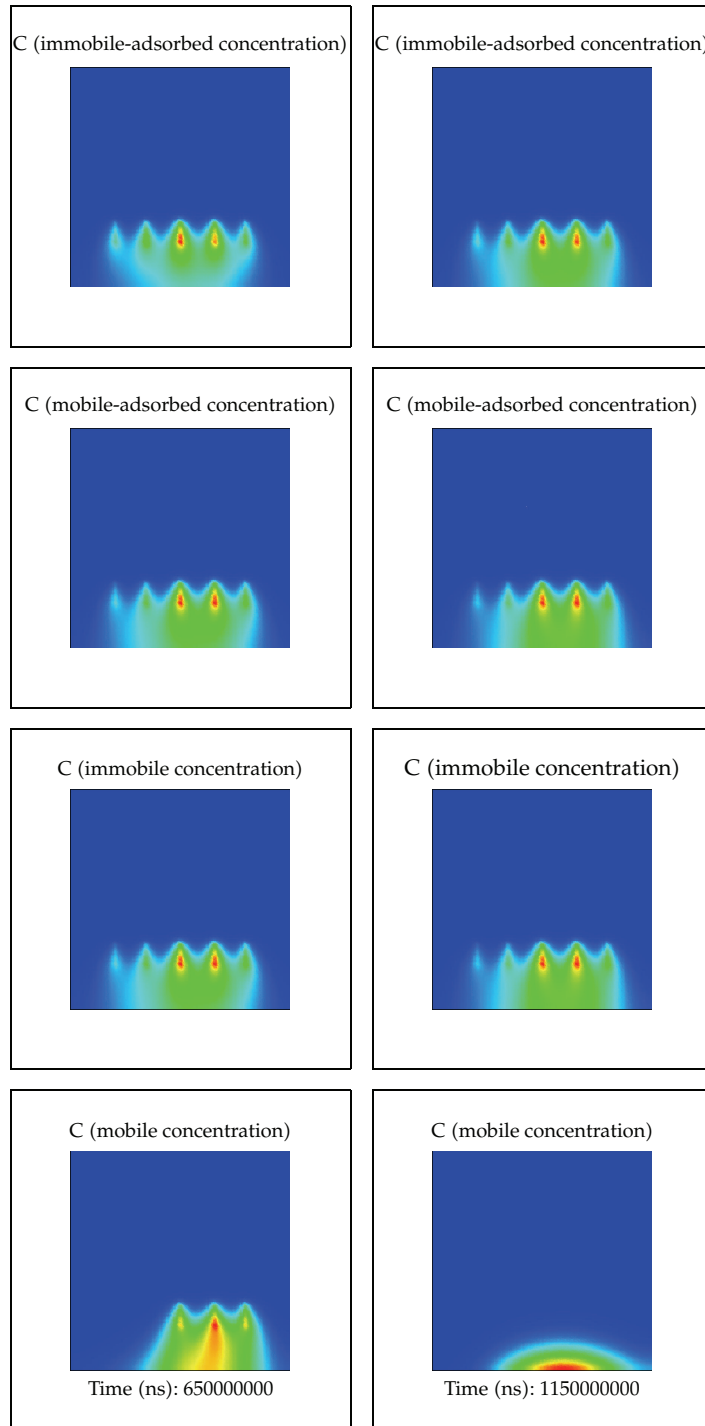
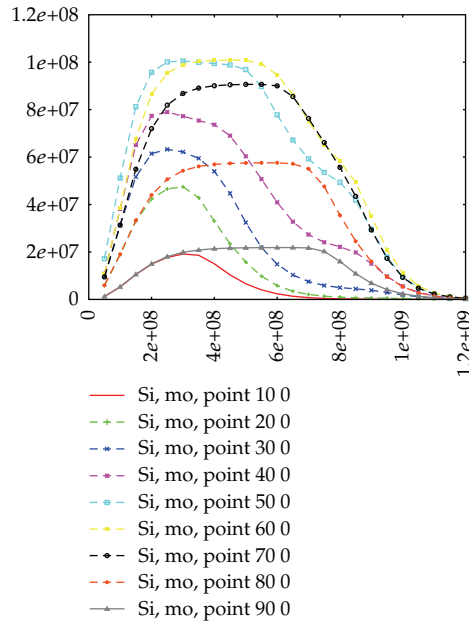
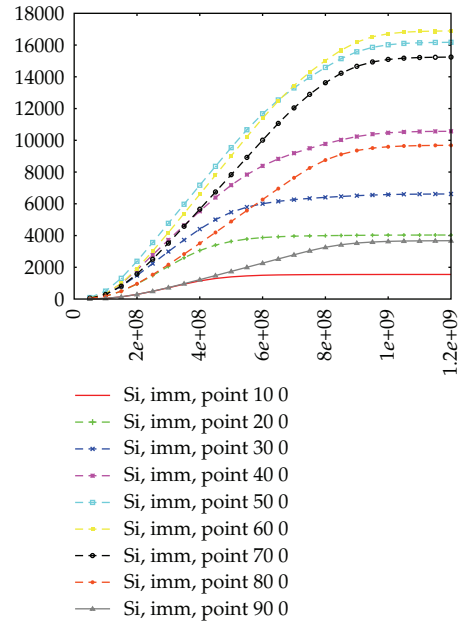


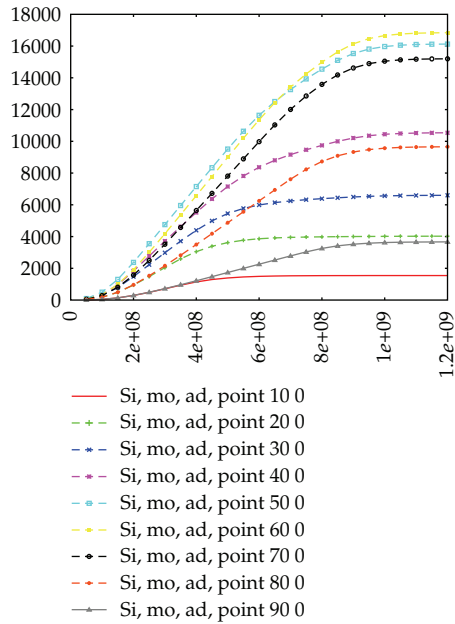
Figure 10: mobile (lowermost), immobile (lower-middle), mobile-adsorbed (upper-middle) and immobile-adsorbed (uppermost) case of 11 moving sources moving with number of time step equal to 15 (left figures) and 25 (right figures), where full concentration is given in red and zero concentration in blue.



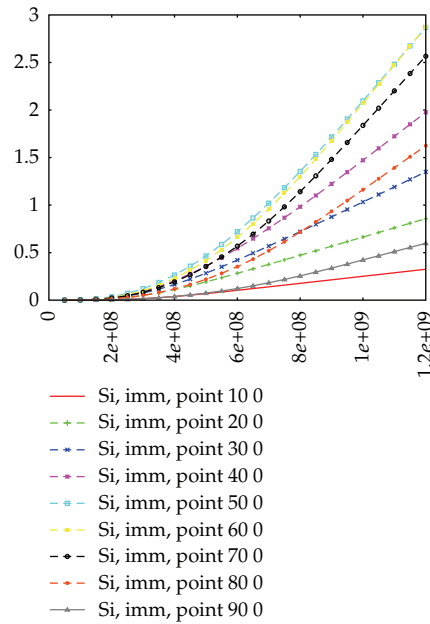
(a)



(b)



(c)



(d)

Figure 11: Deposition rates in four phases: mobile (a), immobile (b), mobile-adsorbed (c), immobile-adsorbed (d) concentration of 11 moving sources moving, (x -axis: time scale in (nsec), y -axis: deposition rate in (mol/nsec)).

We can see in the numerical experiments a loss of the deposition concentration, which means that we have to consider a higher inflow rate of the species. Further, we could verify the underlying model with physical experiments. In the numerical experiments, we presented various ideas to control an optimal deposition process. While numerical experiments are cheap and all possible parameter variations of the model can be done in less than a few weeks, the help in reducing the need for expensive physical experiments is enormous. Such simulations reduce the need for physical experiments and allow of foreseeing new directions of helpful optimizations.

In the future we are interested on analysing such fast processes due to very small time scales, for example, in a nanoscaled models (molecular dynamics model).

References

- [1] V. Hlavacek, J. Thiart, and D. Orlicki, "Morphology and film growth in cvd reactions," *Journal de Physique IV France*, vol. 5, pp. 3–44, 1995.
- [2] J. Geiser and M. Arab, "Simulation of a chemical vapor deposition: mobile and immobile zones and homogeneous layers," *Journal of Porous Media*, vol. 1, no. 2, 2010.
- [3] M. A. Lieberman and A. J. Lichtenberg, *Principle of Plasma Discharges and Materials Processing*, Wiley-Interscience; John Wiley & Sons, New York, NY, USA, 2nd edition, 2005.
- [4] M. Ohring, *Materials Science of Thin Films*, Academic Press, San Diego, Calif, USA, 2nd edition, 2002.
- [5] L. Sansonnens, J. Bondkowski, S. Mousel, J. P. M. Schmitt, and V. Cassagne, "Development of a numerical simulation tool to study uniformity of large area PECVD film processing," *Thin Solid Films*, vol. 427, no. 1-2, pp. 21–26, 2003.
- [6] B. Chapman, *Glow Discharge Processes. Sputtering and Plasma Etching*, John Wiley & Sons, New York, NY, USA, 1st edition, 1980.
- [7] N. Morosoff, *Plasma Deposition, Treatment and Etching of Polymers*, Academic Press, New York, NY, USA, 1st edition, 1990, R. d'Agostino, Ed.
- [8] P. Favia, E. Sardella, R. Gristina, A. Milella, and R. D'Agostino, "Functionalization of biomedical polymers by means of plasma processes: plasma treated polymers with limited hydrophobic recovery and PE-CVD of -COOH functional coatings," *Journal of Photopolymer Science and Technology*, vol. 15, no. 2, pp. 341–350, 2002.
- [9] M. W. Barsoum and T. El-Raghy, "Synthesis and characterization of a remarkable ceramic: ti_3sic_2 ," *Journal of the American Ceramic Society*, vol. 79, no. 7, pp. 1953–1956, 1996.
- [10] Y. Du, J. C. Schuster, H. J. Seifert, and F. Aldinger, "Experimental investigation and thermodynamic calculation of the titanium-silicon-carbon system," *Journal of the American Ceramic Society*, vol. 83, no. 1, pp. 197–203, 2000.
- [11] C. Lange, M. W. Barsoum, and P. Schaaf, "Towards the synthesis of MAX-phase functional coatings by pulsed laser deposition," *Applied Surface Science*, vol. 254, no. 4, pp. 1232–1235, 2007.
- [12] J. Geiser, *Gekoppelte Diskretisierungsverfahren für Systeme von Konvektions-Dispersions-Diffusions-Reaktionsgleichungen*, Ph.D. thesis, Universität Heidelberg, 2003.
- [13] L. Rudniak, "Numerical simulation of chemical vapour deposition process in electric field," *Computers and Chemical Engineering*, vol. 22, no. 1, pp. S755–S758, 1998.
- [14] N. H. Tai and T. W. Chou, "Modeling of an improved chemical vapor infiltration process for ceramic composites fabrication," *Journal of the American Ceramic Society*, vol. 73, no. 6, pp. 1489–1498, 1990.
- [15] J. Geiser, *Decomposition Methods for Differential Equations*, Chapman & Hall/CRC Numerical Analysis and Scientific Computing Series, CRC Press, Boca Raton, Fla, USA, 1st edition, 2009, Magoules and Lai, Ed.
- [16] J. Geiser, "Discretization methods with embedded analytical solutions for convection-diffusion dispersion-reaction equations and applications," *Journal of Engineering Mathematics*, vol. 57, no. 1, pp. 79–98, 2007.
- [17] M. K. Gobbert and C. A. Ringhofer, "An asymptotic analysis for a model of chemical vapor deposition on a microstructured surface," *SIAM Journal on Applied Mathematics*, vol. 58, no. 3, pp. 737–752, 1998.
- [18] J. Geiser and M. Arab, "Porous media based modeling of pe-cvd apparatus: electrical fields and deposition geometries," *Special Topics and Reviews in Porous Media*, vol. 1, no. 3, pp. 215–229, 2010.

- [19] G. Z. Cao, H. W. Brinkman, J. Meijerink, K. J. De Vries, and A. J. Burggraaf, "Kinetic study of the modified chemical vapour deposition process in porous media," *Journal of Materials Chemistry*, vol. 3, no. 12, pp. 1307–1311, 1993.
- [20] H. Rouch, "Mocvd research reactor simulation," in *Proceedings of the COMSOL Users Conference*, Paris, France, 2006.
- [21] T. K. Senega and R. P. Brinkmann, "A multi-component transport model for non-equilibrium low-temperature low-pressure plasmas," *Journal of Physics D*, vol. 39, no. 8, pp. 1606–1618, 2006.
- [22] J. Bear, *Dynamics of Fluids in Porous Media*, American Elsevier, New York, NY, USA, 1st edition, 1972.
- [23] E. Fein, "Software package r^3t ," Tech. Rep., 2004.
- [24] S. Farooq and D. M. Ruthven, "Dynamics of kinetically controlled binary adsorption in a fixed bed," *AIChE Journal*, vol. 37, no. 2, pp. 299–301, 1991.
- [25] V. A. Kadetov, *Diagnostics and modeling of an inductively coupled radio frequency discharge in hydrogen*, Ph.D. thesis, Ruhr Universität Bochum, 2004.
- [26] P. Frolkovič and J. Geiser, "Discretization methods with discrete minimum and maximum property for convection dominated transport in porous media," in *Numerical Methods and Applications*, I. Dimov, I. Lirkov, S. Margenov, and Z. Zlatev, Eds., pp. 445–453, Springer, Berlin, Germany, 2003.
- [27] P. Frolkovič, "Flux-based method of characteristics for contaminant transport in flowing groundwater," *Computing and Visualization in Science*, vol. 5, no. 2, pp. 73–83, 2002.
- [28] P. Frolkovič and H. De Schepper, "Numerical modelling of convection dominated transport coupled with density driven flow in porous media," *Advances in Water Resources*, vol. 24, no. 1, pp. 63–72, 2000.
- [29] I. Farago and J. Geiser, "Iterative operator-splitting methods for linear problems," Tech. Rep. 1043, Weierstrass Institute for Applied Analysis and Stochastics, Berlin, Germany, Mohrenstrasse, Berlin, Germany, 2005.
- [30] E. Hairer, S. P. Nørsett, and G. Wanner, *Solving Ordinary Differential Equations. I*, vol. 8 of *Springer Series in Computational Mathematics*, Springer, Berlin, Germany, 2nd edition, 1992.
- [31] E. Hairer and G. Wanner, *Solving Ordinary Differential Equations. II*, vol. 14 of *Springer Series in Computational Mathematics*, Springer, Berlin, Germany, 2nd edition, 1996.
- [32] P. Bastian, K. Birken, K. Eckstein et al., "Ug-a flexible software toolbox for solving partial differential equations," *Computing and Visualization in Science*, vol. 1, no. 1, pp. 27–40, 1997.
- [33] J. Geiser and M. Arab, "Modelling, optimization and simulation for a chemical vapor deposition," *Journal of Porous Media*, vol. 12, no. 9, pp. 847–867, 2009.

